The Astrophysical Journal, 922:227 (16pp), 2021 December 1 https://doi.org/10.3847/1538-4357/ac2837

Filament Eruption Driving EUV Loop Contraction and Then Expansion above a Stable Filament

Ramesh Chandra[1], Pascal Démoulin[2,3], Pooja Devi[1], Reetika Joshi[1], and Brigitte Schmieder[2,4,5]
[1] Department of Physics, DSB Campus, Kumaun University, Nainital—263 001, India; rchandra.ntl@gmail.com
[2] LESIA, Observatoire de Paris, Université PSL, CNRS, Sorbonne Université, Université de Paris, 5 place Jules Janssen, F-92195 Meudon, France
[3] Laboratoire Cogitamus, 1 3/4 rue Descartes, F-75005 Paris, France
[4] Centre for Mathematical Plasma Astrophysics, Department of Mathematics, KU Leuven, B-3001 Leuven, Belgium
[5] LSUPA, School of Physics and Astronomy, University of Glasgow, UK
Received 2021 March 15; revised 2021 September 15; accepted 2021 September 15; published 2021 December 1

Abstract

We analyze the observations of EUV loop evolution associated with the filament eruption located at the border of an active region (AR). The event SOL2013-03-16T14:00 was observed with a large difference in view point by the Solar Dynamics Observatory and Solar Terrestrial Relations Observatory. The filament height is fitted with the sum of a linear and exponential function. These two phases point to different physical mechanisms such as tether-cutting reconnection and a magnetic instability. While no X-ray emission is reported, this event presents classical eruption features like separation of double ribbons and the growth of flare loops. We report the migration of the southern foot of the erupting filament flux rope due to the interchange reconnection with encountered magnetic loops of a neighboring AR. Parallel to the erupting filament, a stable filament remains in the core of the AR. The specificity of this eruption is that coronal loops, located above the nearly joining ends of the two filaments, first contract in phase, then expand and reach a new stable configuration close to the one present at the eruption onset. Both contraction and expansion phases last around 20 minutes. The main difference with previous cases is that the PIL bent about 180° around the end of the erupting filament because the magnetic configuration is at least tripolar. These observations are challenging for models that interpreted previous cases of loop contraction within a bipolar configuration. New simulations are required to broaden the complexity of the configurations studied.

Unified Astronomy Thesaurus concepts: Solar filaments (1495); Solar flares (1496); Solar coronal loops (1485)

Supporting material: animations

1. Introduction

Solar filaments (or prominences, when observed at solar limb) are cool and dense material plasma suspended in a million degree hot corona (Labrosse et al. 2010; Mackay et al. 2010; Parenti 2014). They are located above the photospheric inversion line (PIL) of the vertical component of the magnetic field. They are observed in the active as well as in the quiet solar atmosphere or between two active regions (ARs). Since the plasma of filaments is about a factor of 100 denser than the coronal plasma it needs to be supported by a force against the action of gravity. The existence of stable support in magnetic dips was initially proposed by Kippenhahn & Schlüter (1957). Present models typically involved a magnetic structure with the filament plasma caught in magnetic dips (see the review by Mackay et al. 2010). Magnetic dips can be present naturally in potential fields with a quadrupolar magnetic configuration but not with a bipolar configuration. Several models have been developed such as the sheared arcade model (Antiochos et al. 1994), and the flux rope (FR) model (Priest et al. 1989; Aulanier & Démoulin 1998; Aulanier & Schmieder 2002). Finally, the existence and the evolution of a filament is strongly linked to the associated magnetic field configuration.

Usually, at some point in their evolution filaments become unstable and erupt. The eruption can be confined by the overlying magnetic field, which is then is called a failed eruption. In the opposite case, the filament, the surrounding coronal magnetic field and the plasma become a coronal mass ejection (CME), which is ejected toward the interplanetary medium (e.g., Gibson & Fan 2006; Chandra et al. 2010; Schmieder et al. 2013; Kliem et al. 2014). Therefore, filament eruptions are thought to play a diagnostic role in the origin of CMEs because of their much higher plasma density than the surrounding corona. Eruptions and associated phenomena, such as the formation of flare ribbons and their separation with time, were initially explained by Carmichael 1964), Sturrock (1966), Hirayama (1974), and Kopp & Pneuman (1976). Later, this two-dimensional model was extended into a three-dimensional model that could explain eruption associated phenomena, including slipping reconnection, circular ribbon formation, and the magnetic shear evolution of flare loops (Aulanier et al. 2010; Janvier et al. 2015).

Different mechanisms could explain the trigger of eruptions, which include the magnetic breakout (Antiochos et al. 1999), tether cutting (Moore & Sterling 2006), kink instability (Török & Kliem 2005), and the torus instability or catastrophe model (Kliem & Török 2006). The observations and models of both the possible pre-eruptive magnetic configurations and the eruption mechanisms have recently been reviewed (Green et al. 2018; Georgoulis et al. 2019; Patsourakos et al. 2020). As the FR is erupting according to the Lin & Forbes (2000) model, a thin current sheet (CS) is formed behind the erupting FR. The erupting FR can be ejected from the corona into the heliosphere thanks to the magnetic reconnection occurring in the CS behind the FR. This reconnection transforms part of the stabilizing magnetic connections passing above the FR to connections located below the FR (flare loops) and to connections wrapped around the FR, so further building the FR.

One of the remarkable phenomenon accompanying solar eruptions is the evolution of coronal loops. This phenomenon is

reported with various spaceborne observations in flare loops with the shrinkage of individual loops while the global loop system expands upward as further flare loops are formed (Forbes & Acton 1996; Sui et al. 2004; Li & Gan 2006; Zhou et al. 2008; Joshi et al. 2009). Moreover, since the launch of the Solar Dynamics Observatory (*S*DO) in 2010, observational evidence of coronal loop contraction and expansion, not associated with flare loops, has been increasing (Gosain 2012; Liu et al. 2012; Sun et al. 2012; Simões et al. 2013; Zhou et al. 2013; Shen et al. 2014; Dudík et al. 2017; Wang et al. 2018; Dudík et al. 2019; Devi et al. 2021). This is a consequence of SDO continuous high temporal and spatial resolution observations. This phenomenon is usually observed together with eruptive solar flares. These loops are already present before the flare, so they are different from flare loops that are formed by reconnection during the flare. The speed of the contraction and expansion is typically between a few and 40 km s^{-1}. Furthermore, in some cases the contracted loops end up oscillating (e.g., Gosain 2012; Liu et al. 2012; Simões et al. 2013).

To explain the phenomena of the loop contraction two mechanisms were explored. The first mechanism is the *magnetic implosion* conjecture proposed by Hudson (2000). According to this, the energy generated during a solar eruption has its origin in the implosion of the magnetic configuration in a nearby part of the corona. The expansion followed by contraction in coronal loops is recently simulated in 3D by Wang et al. (2021). The physical interpretation of such implosion has later changed. For example, Simões et al. (2013) interpret the observed loop contraction with an implosion that is a consequence, and not a driver, of the energy release during the event. Later, Russell et al. (2015) interpreted the loop contraction as the consequence of the reduction of the magnetic pressure due to the magnetic reconnection occurring in the flare. Several observations of loop contraction are interpreted as supporting this mechanism (Wang et al. 2018). The second mechanism is proposed by Aulanier et al. (2010) and Zuccarello et al. (2017). This model is based on the 3D magnetohydrodynamics (MHD) numerical simulations of the formation then eruption of an FR in a bipolar magnetic configuration modeling an AR configuration. According to their model, the loop contraction/expansion is the result of the vortex forming on both sides of erupting FR legs. These vortex flows drive the coronal loops and as a result of this the contraction/expansion in the loops observed, depending on where the loops are in the vortex. The careful analysis of the contraction/expansion of loops in some studied eruptions' filament support the conclusion of the MHD simulations (Dudík et al. 2017, 2019; Devi et al. 2021).

Coronal loops can also be excited by propagating coronal waves, in particular fast magneto-acoustic waves (Wills-Davey & Thompson 1999; Ballai 2007; Ballai et al. 2008). These waves can be generated by a sudden energy release process like the phenomena of solar flares and CMEs. The propagation of coronal waves can be considered as a freely propagating wavefront that is observed to interact with coronal loops (see, e.g., Wills-Davey & Thompson 1999; Ballai et al. 2008).

In this paper, we study loop contraction and expansion associated with a filament eruption on 2013 March 16 observed in EUV wavelengths by the Atmospheric Imaging Assembly (AIA) imager on board SDO and by EUVI on board the Solar Terrestrial Relations Observatory (STEREO) with a large difference in viewing points. The specificity of this event is that the loop contraction and expansion were occurring not only in coronal loops located nearby the endpoint of the erupting filament, but also in loops located over a stable filament. This filament is located on the side of the erupting one with a nearly parallel orientation of most parts of both filaments, which are also nearly joining at one end. Then, this is an interesting eruption to study as it broadens the range of configurations where the loop contraction and expansion could occur. The layout of this paper is as follows: Section 2 describes the data sets, the morphology of filament eruption, the history of the magnetic configuration of the involved AR, the kinematics of the eruption, and the observational results related to EUV loop contraction and expansion. The physical interpretation of the obtained results is given in Section 3. Finally, in Section 4, the conclusion of the study is given.

2. Observations

2.1. Overview of the Event

The filament eruption on 2013 March 16 was observed by the AIA (Lemen et al. 2012) on board SDO, Pesnell et al. 2012) at different EUV wavelengths with pixels of 0.6″ and cadence of 12 s. For our present analysis, we used the AIA data of 304, 171, 193, and 211 Å. which correspond to the wavelengths where the eruption is observed the best. For the magnetic configuration of the filament region, we analyzed the photospheric magnetic field line-of-sight data of Helioseismic Magnetic Imager (HMI; Schou et al. 2012). The pixel resolution and the temporal resolution of the HMI magnetic field data is 0.5″ and 45 s, respectively. The eruption was also observed by the Solar Terrestrial Relations Observatory Ahead (STEREO A, Howard et al. 2008) spacecraft with a cadence of 10 minutes. All the above mentioned data are processed by the solar soft package. To remove the solar rotation, we rotated all used AIA analyzed images at 12:30 UT. For this purpose, we used the "drot_map" routine available in solar soft. In order to enhance the contrast of the AIA data, we processed the images with the multi-Gaussian normalization (MGN) method developed by Morgan & Druckmüller (2014). To further outline the evolution we create base-difference movies, both with and without the MGN method, with the base time set at 12:30 UT.

The erupting filament (Fil_1) on 2013 March 16 was located at the northwest border of the NOAA AR 11690 (Figure 1(g)). A second stable filament (Fil_2) is present on the main PIL of AR 11690. Both filaments are indicated with arrows in Figures 1(a) and (d). The evolution of the erupting filament Fil_1 in AIA 304, 171, 193, and 211 Å is summarized with three selected times in Figure 1. The accompanying movies provide a detailed view of the eruption. The filament started to move upwards at ≈13:19 UT in the northwest direction (best seen with base-difference movies). Much later, at about 13:59 UT, two flare ribbons started to develop below the erupting filament. The double ribbons, indicated by arrows in Figure 1(b), are well observed in 304, 171, 193, and 211 Å. As the filament was moving upward, the double ribbons separated from each other as predicted in the standard flare model (Section 1). Furthermore, J-shaped ribbons are present after 14:29 UT, which indicate the eruption of an FR (Démoulin et al. 1996; Aulanier et al. 2010). These ribbons are best seen in the base difference of AIA 304 Å.

The MGN technique is applied to AIA data in order to enhance the coronal structures so that the morphology and the dynamics of the eruption could be better understood. Figure 2

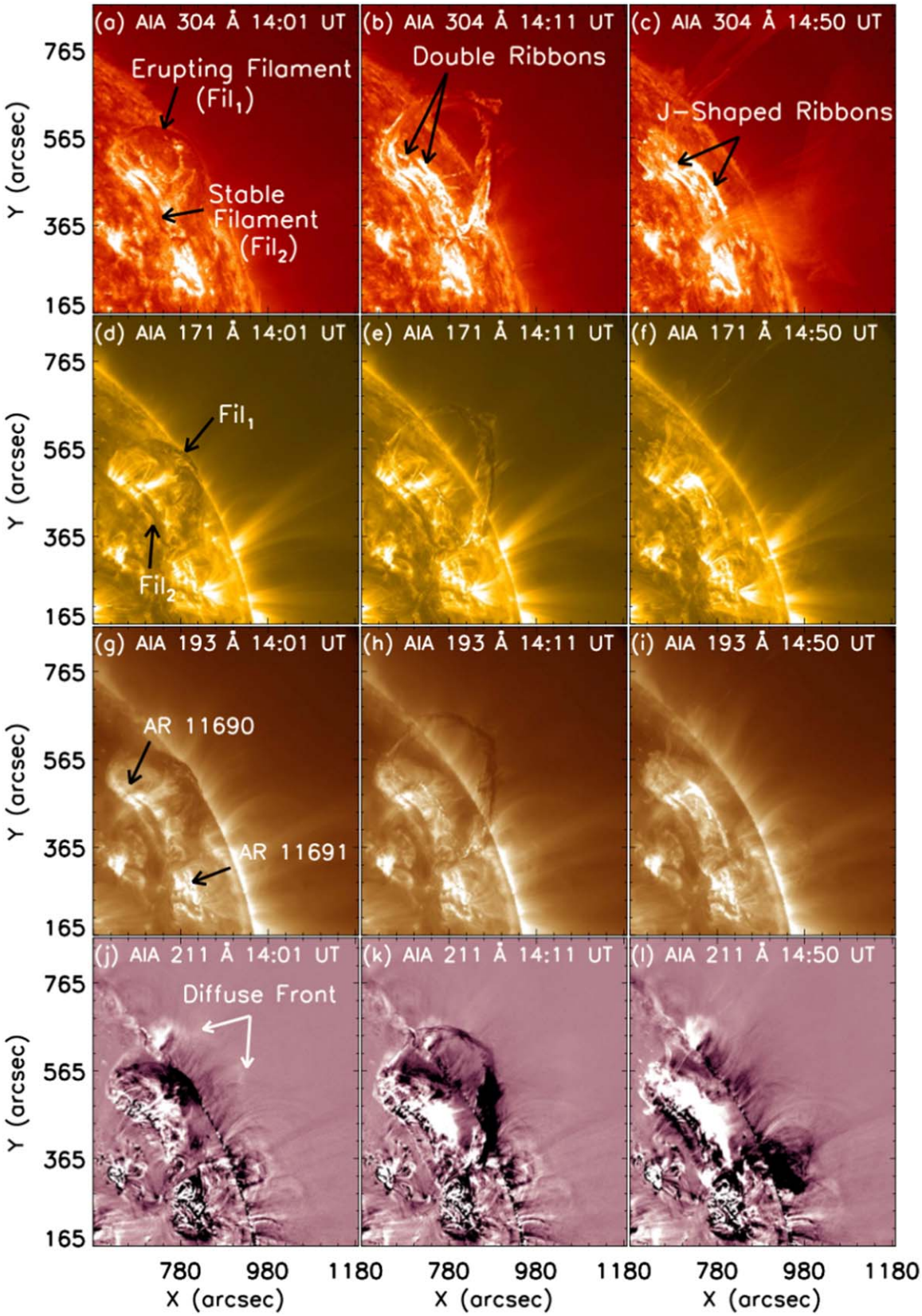

Figure 1. Multiwavelength view of the filament eruption of 2013 March 16 in AIA 304, 171, 193, and 211 Å. The AIA 211 Å images are base difference images (base time: 12:30 UT). The location of the erupting filament (Fil_1), the stable filament (Fil_2), and the flare ribbons are indicated in panels (a), (d) and (b), (c), respectively. The AR involved in the eruption, AR 11690, and the southern one are indicated in panel (g). The propagating diffuse front above the filament is shown in panel (j). An animation of this figure is available. The animation starts at 12:30 UT and end at 15:00 UT. The real-time duration of the animation is 25 s.

(An animation of this figure is available.)

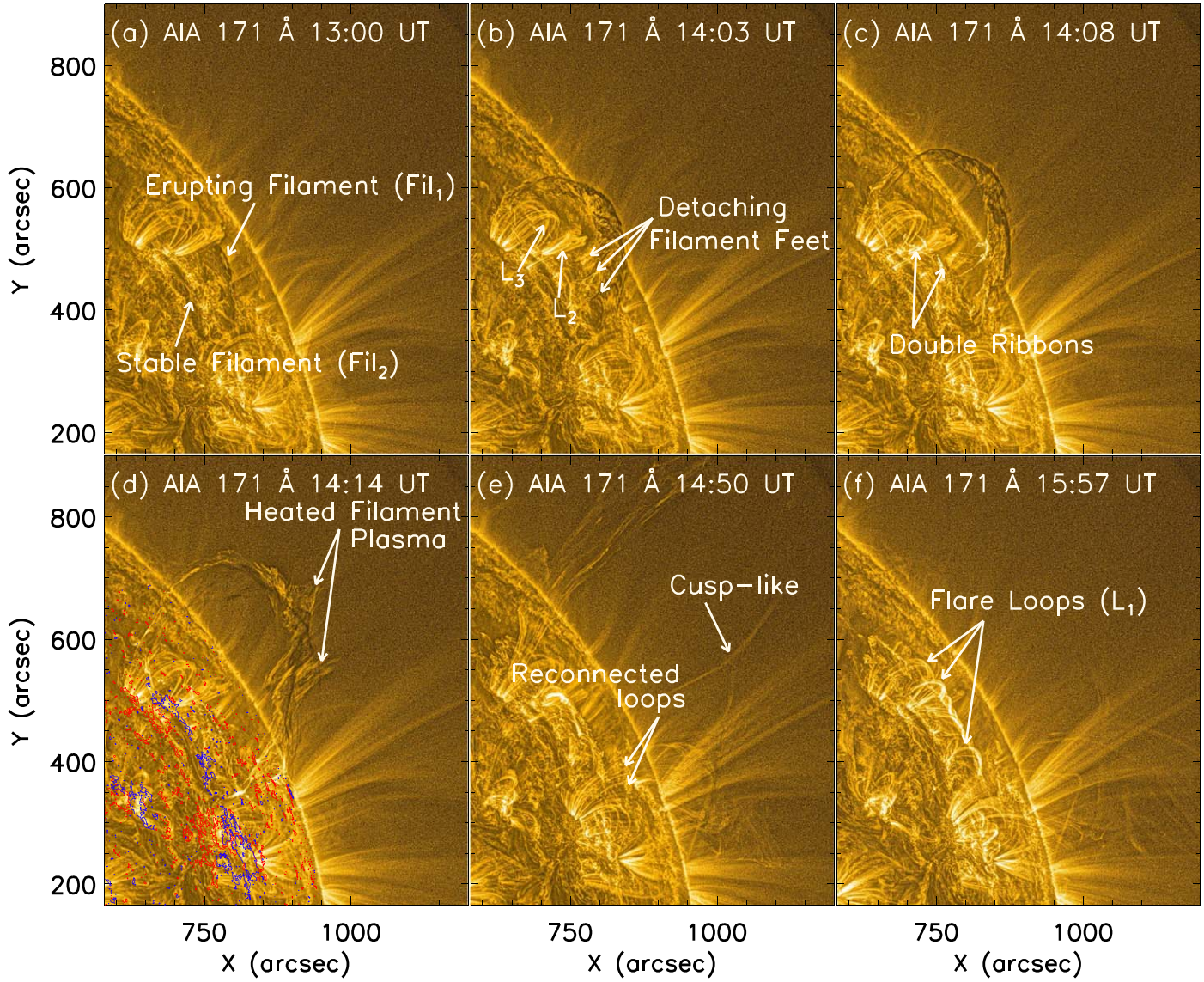

Figure 2. Evolution of the filament eruption with AIA images at 171 Å processed with the MGN method (Section 2.1). The erupting (Fil_1) and the stable (Fil_2) filaments are indicated in panel (a). Specific characteristics of the erupting filament are pointed in panels (b) and (d). The consequences of the main energy release are indicated in panels (c) and (f) with flare ribbons and flare loops (L_1), respectively. The HMI positive/negative polarity contours are overlaid in panel (d) with red/blue contours (contour level: ±30 G). The loop systems L_2 and L_3, located above Fil_2, are indicated in panel (b). The reconnected loops, marked in panel (e), are due to the reconnection of the southern leg of the erupting FR with the magnetic field of AR 11691 (located southward of AR 11690, see Figure 1(g)). An animation of this figure is available. The animation starts at 12:30 UT and end at 15:00 UT. The real-time duration of the animation is 25 s.

(An animation of this figure is available.)

shows the evolution with the MGN technique applied to 171 Å. Arrows point to the main observational features. The filament eruption is observed the best with the 171 Å filter with more contrasted images, which reveal both the EUV absorption by the dense and cold filament plasma and the emission of heated plasma (e.g., part of the filament, flare ribbons, and loops).

On mid-2013 March 16 the filament Fil_1 erupted as a coherent structure. This is emphasized by a sharp leading edge moving as a coherent entity (Figures 2(a)–(c)). At the beginning of the filament eruption three dark features are extending below the filament body. They are pointed by three arrows in Figure 2(b). These extensions are filament feet/barbs which have been identified previously mostly in quiescent filaments (Aulanier et al. 1999; Mackay et al. 2010). As the eruption progresses, the feet of the filaments become more clearly visible, before getting split with the lower part falling toward the chromosphere and with the upper part being integrated into the eruptive configuration. During this splitting, the associated plasma is changing from absorption to emission, so it is heated. They are both indications that magnetic reconnection occurs below the erupting FR.

As the filament erupts, its two ends stay anchored at low heights (Figures 2(a)–(d)). This allows us to identify the two footpoints of the erupting FR, which are located in the northward and west-southward periphery of AR 11690, in negative and positive photospheric polarities, respectively (Figure 3(d)). Later in the eruption, a cusp-like shape appears in emission in 171 Å (Figure 2(e)). However, the temporal evolution is more compatible with the crossing in the projection of two loops (see associated movie).

The evolution of the southern part of the erupting filament is complex (see attached movies in 304, 171, 193, and 211 Å).

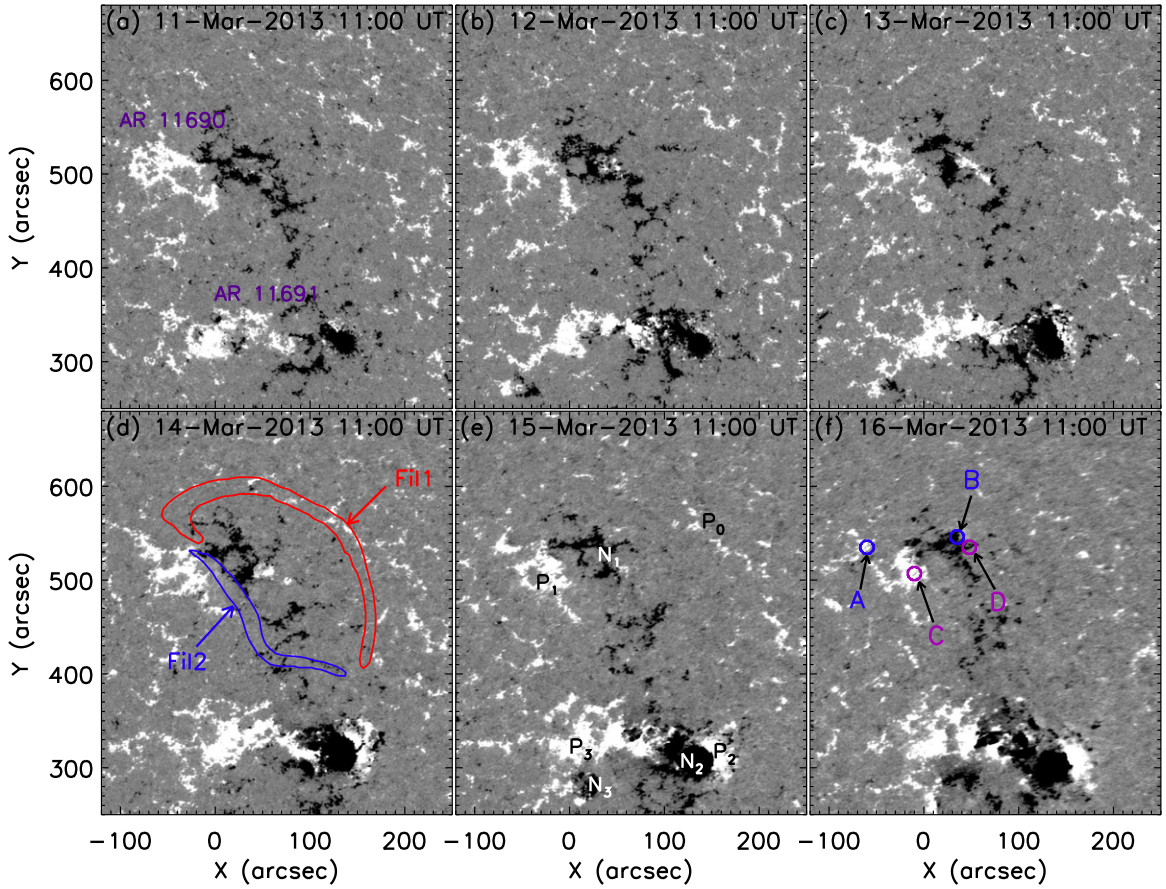

Figure 3. Evolution of the longitudinal component of the photospheric magnetic field the ARs 11690 and 11691. The observations are derotated to the central meridian location. The contours in panel (d) delimitate the location of the two filaments observed in Hα. The red contour indicates the erupting filament Fil_1, while the blue contour indicates the stable filament Fil_2. The different magnetic polarities are named by P_0 (remnant field of a previous AR), P_1, N_1 (AR 11690), P_2, N_2, P_3, N_3 (AR 11691). The locations of the loop footpoints, defined in Figure 6(b), are indicated by the pairs A, B, and C, D, respectively in panel (f). An animation of this figure is available. The animation runs from 2013 March 11 00:00 UT to 2013 March 16 17:00 UT with a real-time duration of 22 s.

(An animation of this figure is available.)

We interpret this evolution as the reconfiguration of the southern FR leg. During its upward ejection, the FR expands and reconnects, at least partially, with the main bipolar field of AR 11691. This shifts the FR magnetic anchorage from the positive polarity in front of AR 11690 to the positive following polarity of AR 11691 as traced by the new connections pointed in Figure 2(e) (with *Reconnected Loops*). A part of the dense filament plasma falls along and fill partly these new connections as seen the best in 171 and 304 Å base-difference movies. We conclude that the lateral drift of the filament foot is accomplished via interchange reconnection with encountered southern magnetic loops. These observations are globally consistent with the previously reported observations of such lateral drift of the foot of an erupted prominence/filament (Hori 2000; van Driel-Gesztelyi et al. 2014; Dudík et al. 2019; Lörinčík et al. 2019; Zemanová et al. 2019). Another part of the erupted filament drains to the end region of the J-shaped flare ribbon in the west (toward polarity P_0 in Figure 3), which is near the periphery of the FR leg. This is best seen in AIA with higher temperatures, e.g., 211 and 193 Å, and it implies that the magnetic configuration of this filament leg splits.

The flare associated with this filament eruption is weak as it does not saturate the EUV detectors. Indeed the GOES instrument does not observe any flux enhancement in X-rays, then this event is not classified as an X-ray flare. Still, it presents all the EUV characteristics of a two ribbons flare with two separating ribbons and an arcade of flare loops, L_1, linking them (Figures 2(c), (f)). Both these ribbons and flare loops are partly hidden by other sets of loops, L_2 and L_3, located in front of the AIA images (Figure 2(b)). These L_2 and L_3 sets are not part of the flare, which is associated to Fil_1 eruption. Rather these L_2 and L_3 sets are located over the stable filament Fil_2, and they are studied in Section 2.4.

2.2. Magnetic Configuration

The evolution between 2013 March 11 and 16 of the magnetic field in the vicinity of the filaments is displayed in Figure 3 in the local solar frame. The main magnetic polarities are labeled in panel (e). AR 11690 is mostly in a decaying stage, with the emergence of a bipole in its negative polarity N_1 (Figures 3(b)–(d)). This induced a reorganization of its leading polarity from March 12–14. More importantly, long-term small scale cancellations of the magnetic flux are observed at the PIL between N_1 and P_0 (this is best seen in the associate movie). These cancellations are induced by the dispersion of the magnetic polarities due to sub-photospheric convection motions with a timescale of days. This flux cancellation is expected to build the FR, which supports the filament (van Ballegooijen & Martens 1989). It is also at the origin of the

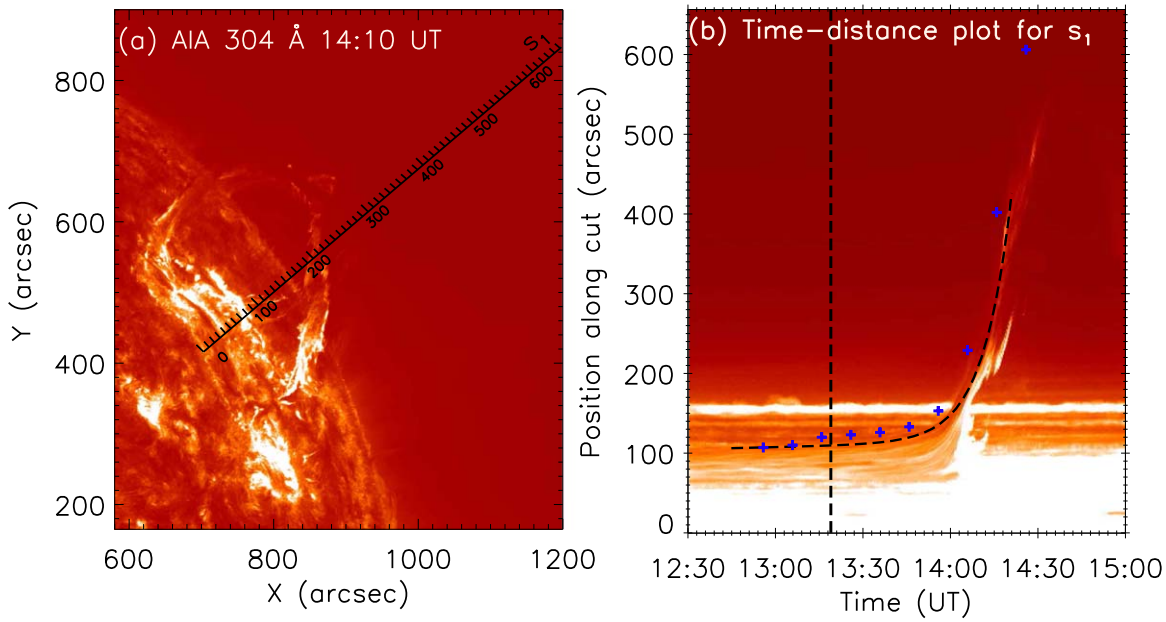

Figure 4. (a) AIA 304 Å image with the location of slice S_1 used for the analysis of the filament Fil_1 height-time evolution. (b) Height-time plot along the slice S_1. The height is corrected from solar rotation. The vertical dashed line indicates the approximate onset time of the filament eruption. The black dashed line is the fit of Equation (1) to the filament apex as traced with the AIA 304 Å data along slice S_1. The blue crosses represent the apex height of the filament leading edge derived by triangulation with the data of SDO/AIA and STEREO A/EUVI (see Figures 1 and 5). The height is set at the same position for the first blue cross. During the eruption these heights are slightly above the AIA 304 Å apex and its fit with Equation (1) due to a projection effect.

slow evolution of the magnetic configuration which can bring it to instability (Amari et al. 2010; Aulanier et al. 2010).

The erupting filament Fil_1 is located at the northwest side of the AR 11690 as shown with the red contour of Hα observation co-aligned with the magnetogram (Figure 3(d)). More precisely the bottom of the Hα filament is following the PIL between the AR negative leading polarity N_1 and a dispersed large-scale positive polarity P_0 (the remnant of an earlier AR). The filament extends on the positive polarity indicating that it is inclined toward the west. The explanation for the westward inclination of the filament Fil_1 away from its underlying PIL is the asymmetry of the magnetic field strength on both sides of the PIL. This inclination is present in MHD simulation during the equilibrium phase and even more visible during the eruption phase (Aulanier et al. 2010; Török et al. 2011; Titov et al. 2018, 2021). From coronal observations, such asymmetry is also known to cause eruptions to be inclined toward the weak-field side (e.g., Panasenco et al. 2013; Kay et al. 2015). Next, a narrow stable filament, Fil_2, is located along the main PIL within AR 11690 (blue contour in Figure 3(d)). The filament Fil_2 follows well the local PIL and it is narrower than Fil_1 as typically observed for filaments within ARs compared to filaments at the periphery of ARs. Furthermore, both filaments, Fil_1 and Fil_2, are on the same PIL located around the polarity N_1. Fil_1 is even curving slightly inside AR 11690 in its northern part (Figure 3(d)).

As mentioned in Section 2.1, the shape of the observed ribbons is reverse J-shaped. Such orientation of the ribbons is evidence of left handedness in the AR (Démoulin et al. 1996; Williams et al. 2005; Chandra et al. 2009). Based on this, we infer the handedness of Fil_1 is left handed. Another method to determine the handedness of the filament is as follows. We have identified the magnetic polarities at the end points of filament Fil_1 and found that the northern/southern footpoints are located in positive/negative polarities, respectively (Figure 3(d)). In addition to this, the eastern/western side of the filaments are in negative/positive polarities, respectively. Using these identifications, we have determined the handedness of the filament (see Figure 5 of Mackay et al. 2010) and have concluded that the filament F_1 has a left-handed configuration. The same method is applied for the filament F_2, which is also found to be in a left-handed configuration. However, this correspondence of handedness is not sufficient to infer that both filaments are in a single magnetic configuration along the same PIL. We found during the quiet phase, before 12:40 UT on March 16, it is difficult to find a separation between the two filaments. However, the eruption of Fil_1 and not of Fil_2 is a clue supporting separated magnetic field configuration, with the limitation that filament plasma outlines only a small fraction of the magnetic configuration. Then, we will first consider below two nearly parallel filaments, before coming back in Section 3.2 to the details of this northern part of the PIL where they are nearby.

Finally, another AR, NOAA 11691, is developing southward to AR 11690 and with the same global bipole orientation (P_3-N_2, Figure 3). Since AR 11691 is nearby AR 11690 and the erupting magnetic structure is strongly expanding southward, the coronal field of AR 11691 partly reconnects with the erupting magnetic field (see Figure 2(e), related movie, and Section 2.1).

2.3. Eruption Kinematics

We explore the eruption kinematics using AIA data sets. A global and qualitative view of the eruption is given by the three movies attached to Figure 1. A quantitative analysis is done with the slice S_1 shown in Figure 4(a). We define the location of slice S_1 in AIA images to follow the filament leading edge. The measured height is corrected from solar rotation. While the filament eruption and its consequences are best seen with 171 Å data, the early part of the eruption is partly masked with the sets L_2 and L_3 of coronal loops present in front of the erupting

filament (middle left of Figures 2(a), (b)). These loops are not emitting in 304 Å, then we privilege this filter to study the pre-eruption phase, as well as the whole filament eruption, while we also apply the same method to the other filters for completeness.

The kinematics of the filament eruption is an important clue for understanding the triggering mechanism of the eruption. Therefore, in order to analyze the kinematics of the filament eruption, we visually select points along the bright tracks of the time-distance plots as shown in Figure 4(b). Cheng et al. (2020) have analyzed 12 eruptions and tested several functions to fit the data. They found that the combination of linear and exponential time dependencies provide the best description of the full data set, and therefore the lowest χ^2 for most eruptions, compared to previously suggested functions (like a power law of time). The most general equation analyzed by Cheng et al. (2020) is

$$h(t) = a\ e^{b(t-t_0)} + c\ t + d. \quad (1)$$

Here, we note that t_0 is a redundant parameter as the first term can be rewritten as $a\ e^{-bt_0}e^{bt} = a'e^{bt}$ so that all the combinations of the three parameters a, b, t_0, which provides the same a' value, define exactly the same function. Said differently, b is defined by the temporal behavior of the data while changing a in Equation (1) could be exactly compensated by changing t_0. Then, we fix t_0 to a given value, 12:45 UT as Cheng et al. (2020) fixed it to their first data point. The coefficients a, b, c, and d are determined by minimizing the reduced χ^2, χ^2_r, between the data and Equation (1) The fitting is done using the mpfit routine available in the solar software (SSWIDL). The goodness of the fitting is given by the reduced χ^2_r value obtained. The χ^2 is defined by $\chi^2 = \sum_{i=1}^{N} [h_i(t) - H_i(t)]^2$, where h_i and H_i are the fitting and measured heights, respectively, and t is the time. This formula is slightly different than the one used by Cheng et al. (2020) since we are not including the error for each measured height (the minimum found assumed the same error for each measurement). Finally we calculated the reduced χ^2_r value as $\frac{\chi^2}{\mathrm{DOF}}$, where DOF is the number of the degree of freedom. We find the minimum $\sqrt{\chi^2_r} = 1\farcs4$. This is only slightly above two pixels of AIA ($1\farcs2$), indicating that Equation (1) provides a close representation of the data.

During the earlier times of Figure 4(b), a slow linear increase of the filament height is present, defined as the slow-rise phase by Cheng et al. (2020). The fit of Equation (1) to the data provides $c \approx 2$ km s^{-1} in all AIA channels. This slow-rise phase is typically associated with the presence of weak brightenings. They are interpreted as the consequence of tether-cutting reconnection, which allow the slow upward motion. Later, during the acceleration phase, the speed of the eruption increases exponentially. The maximum speed of the eruption was computed by derivating the height-time fit of the data. The calculated maximum speed reached up to 300 km s^{-1} within the AIA field of view. This increase occurs on the timescale $1/b \approx 9.6$ minutes. This exponential behavior is characteristic of the linear development of an instability.

The beginning of the eruption is difficult to define precisely as the filament top is smoothly changing from a linear to an exponential rise. Also, there is no characteristics time defined by Equation (1) as t_0 is an ill-defined parameter (see above), and then cannot be associated with an onset time. Indeed, for neither linear and exponential behaviors there is no specific time that can be referred to (said differently both functions can be shifted in time while keeping the same form). Then, extra information needs to be added to define the beginning of the eruption from Equation (1) The instability starts at least before the exponential rise is large enough to be detected. This is best quantified with the velocity, $a\,b\,e^{bt}$ becoming larger than a threshold value v_t. Then, the eruption start time is defined as

$$t_{\mathrm{start}} = \frac{1}{b}\ln\left(\frac{v_t}{a\,b}\right). \quad (2)$$

Taking $v_t = c$ sets the exponential velocity equal to the linear velocity, so the growth of the instability is well visible above the linear rise. This occurs at ≈13:30 UT. The eruption is expected to start even earlier. The exponential is well detectable over the fluctuations of the slow-rise phase when it is larger than three times the standard deviation, which is found to be ≈0.62 km s^{-1}. Including this velocity as v_t in Equation (2) defines the eruption as having started at 13:19 UT, so 11 minutes before. This last time is expected to be closer to the real eruption start, which is expected to be even earlier on when the exponential was too small to be detectable. To be conservative, we set the starting time at 13:19 UT.

The eruption was also well observed by the STEREO A spacecraft with a different viewing angle in longitude. The angle between the STEREO A and the SDO on 2013 March 13 was 130° and for STEREO A the filament was located close to the eastern limb. The evolution of the eruption in 304 Å is shown in Figure 5. The arrow points to the leading edge apex of the eruption. This leading edge is a smooth bent curve at the beginning of the eruption as with SDO observations (Figures 1 and 2). The appearance of the filament feet below the filament is partly different than the ones observed by AIA because STEREO A observes the other side of the filament. As the eruption proceeds, the filament becomes bright both because of plasma heating, as described above for AIA observations, and because the plasma is observed over the limb with a weaker emitting background, so as a prominence. Next, a large quiescent prominence is present in the background at the eastern limb (Figure 5). This corresponds to an extended filament, about one solar radius long, located between the diffuse eastern extension of the positive polarity of AR 11690 (well outside the field of view of Figure 3) and another large-scale and diffuse negative polarity located further to the East. No significant consequence of the eruption of Fil_1 is observed on this large quiescent filament (Figure 5).

By combining the data of AIA 304 Å and STEREO A 304 Å data, these stereoscopic observations allow deriving the true height of the filament. The location pointed by the arrow in Figure 5 is taken for the computation of the filament top height using the trigonometric triangulation method "*ssc_measure*" available in solar soft. The points selected for the height-time plot in the triangulation method are along the direction of slice S_1 for AIA observations. This provides us an opportunity to compare the calculated speeds derived by the time-distance analysis and the stereoscopic analysis. For the comparison of the height derived from the triangulation method and from the AIA time-distance analysis, the common height reference is set before the eruption at the top of the filament. The calculated heights are overplotted on the time-distance plot of Figure 4(b) with the blue "+" symbol. Using these points, we compute a

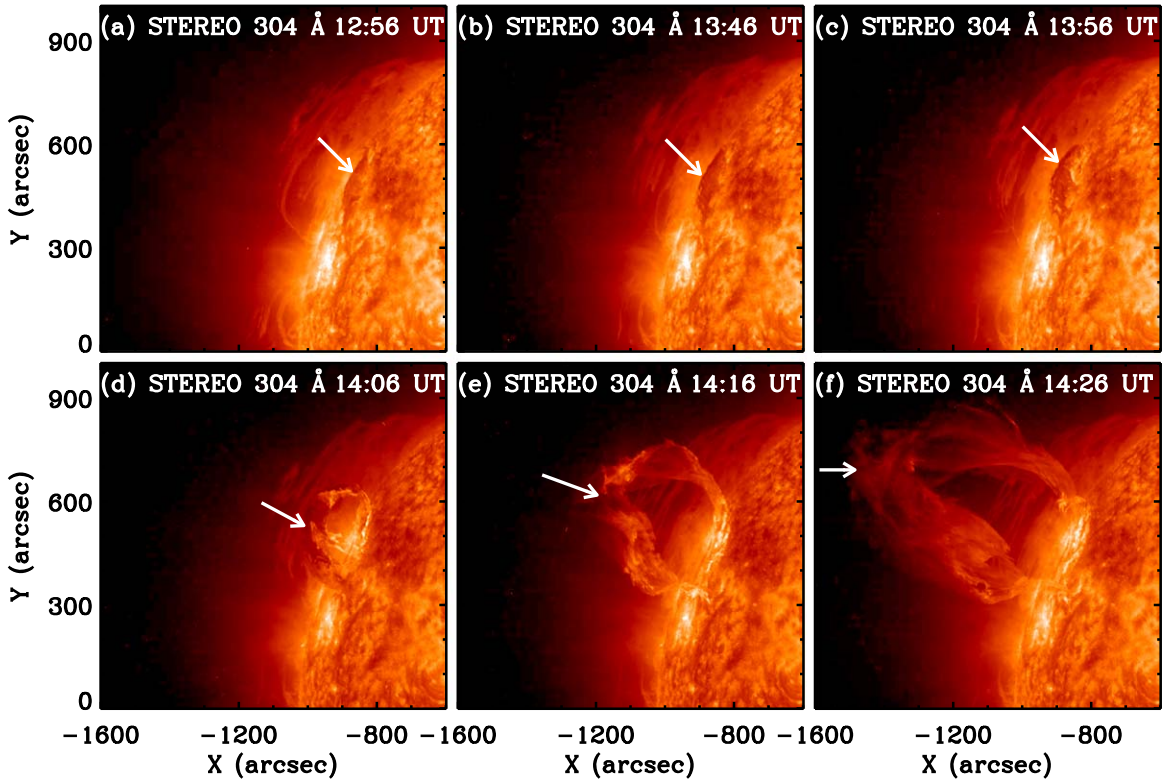

Figure 5. Evolution of the filament observed by STEREO A /EUVI in 304 Å at the eastern solar limb. The view point is on the other side of the filament as observed with AIA (Figure 4(a)) with a longitude difference of 130° between the spacecraft. The filament/prominence leading edge apex is indicated by arrows.

mean speed of ≈180 km s^{-1}. This derived speed from triangulation methods is about 20% faster than the speed derived from the time-distance analysis of the AIA data. This difference is due to projection effects as the velocity measured with AIA does not include the velocity component out of the plane of the sky.

Finally, the filament eruption produced a CME observed by the Solar and Heliospheric Observatory/Large Angle and Spectrometric Coronagraph Experiment (LASCO) in the north-west direction. In the LASCO C2 field of view, the CME appears at ≈14:48 UT at a height of 4 $R_\odot$ and it is visible in the LASCO C3 field of view up to ≈25 $R_\odot$ at 19:54 UT. The CME was a partial halo having a projected width of 323°. The measured mean speed within C2 and C3 fields of view is ≈790 km s^{-1} (see https://cdaw.gsfc.nasa.gov/CME_list), then the ejection was further accelerated compared to the above measurements in the low corona.

2.4. Loops Contraction and Expansion

In this section, we analyze the EUV loop contraction and expansion related to the eruption of the filament Fil$_1$ on 2013 March 16. We will not study the shrinkage of flare loops L$_1$ as this phenomena was already well studied (see Section 1) but rather the evolution of coronal loops that are not involved in the flare reconnection. This phenomena is observed with 171 and 193 Å filters in two sets of loops (Figure 6). We name these two loop systems as L$_2$ and L$_3$, respectively, as indicated in Figures 2(b) and 6(c). Both loop systems are rooted in P_1 (positive) and N_1 (negative) polarities (Figure 3(e), (f)) of AR 11690. The location of STEREO A compared to SDO is suited for a triangulation, as done above for Fil$_1$; however, this is not possible for the loops of L$_2$ and L$_3$ as they are hidden behind the filament Fil$_1$ (Figure 5).

The eastern set, L$_3$, is better observed with loops seen from one side, nearly face-on, and they are well defined over their full length. These loops are located above the location where filament Fil$_1$ and Fil$_2$ are nearly joining (Figures 6(b), (c)). They end on both sides of these filaments (Figures 3(d), (f)). The geometry of the western set L$_2$ is more difficult to define from AIA observations since the direction of observation is nearly along the loops (side-on). Moreover, the part closer to the observer is faint, and the emitted light is mixed with the one of the backgrounds coming from the stable filament Fil$_2$ and its surrounding brightenings. Still, the bottom part of these legs of the loop system L$_2$ can be seen on the front side of the filament Fil$_2$. Then, the loops L$_2$ are rooted on both sides of filament Fil$_2$, as the loop system L$_3$ (Figures 3(d), (f)). The corresponding co-aligned photospheric magnetograms, e.g., Figure 2(d), on March 16 confirm that both sets of loops are rooted in the magnetic polarities surrounding the stable filament and the end of the erupting one. With a space filling coronal magnetic field (low plasma β conditions), L$_2$ and L$_3$ belong to the same magnetic arcade passing over Fil$_2$ and extending all along polarities P_1 and N_1. The heating is probably not large enough in the arcade middle to create dense enough coronal plasma, then there is a gap of coronal emission and the appearance of two separate sets of loops. We conclude that these two sets of loops belong to the magnetic arcade that overlays the stable filament Fil$_2$ outlined with a blue contour in Figure 3(d) and ends above the northern end part of filament Fil$_1$.

The evolution of these loops during the filament eruption is shown in Figure 6 at four times with the AIA 171 Å filter. We have drawn two straight lines at the top of the loops at 13:00

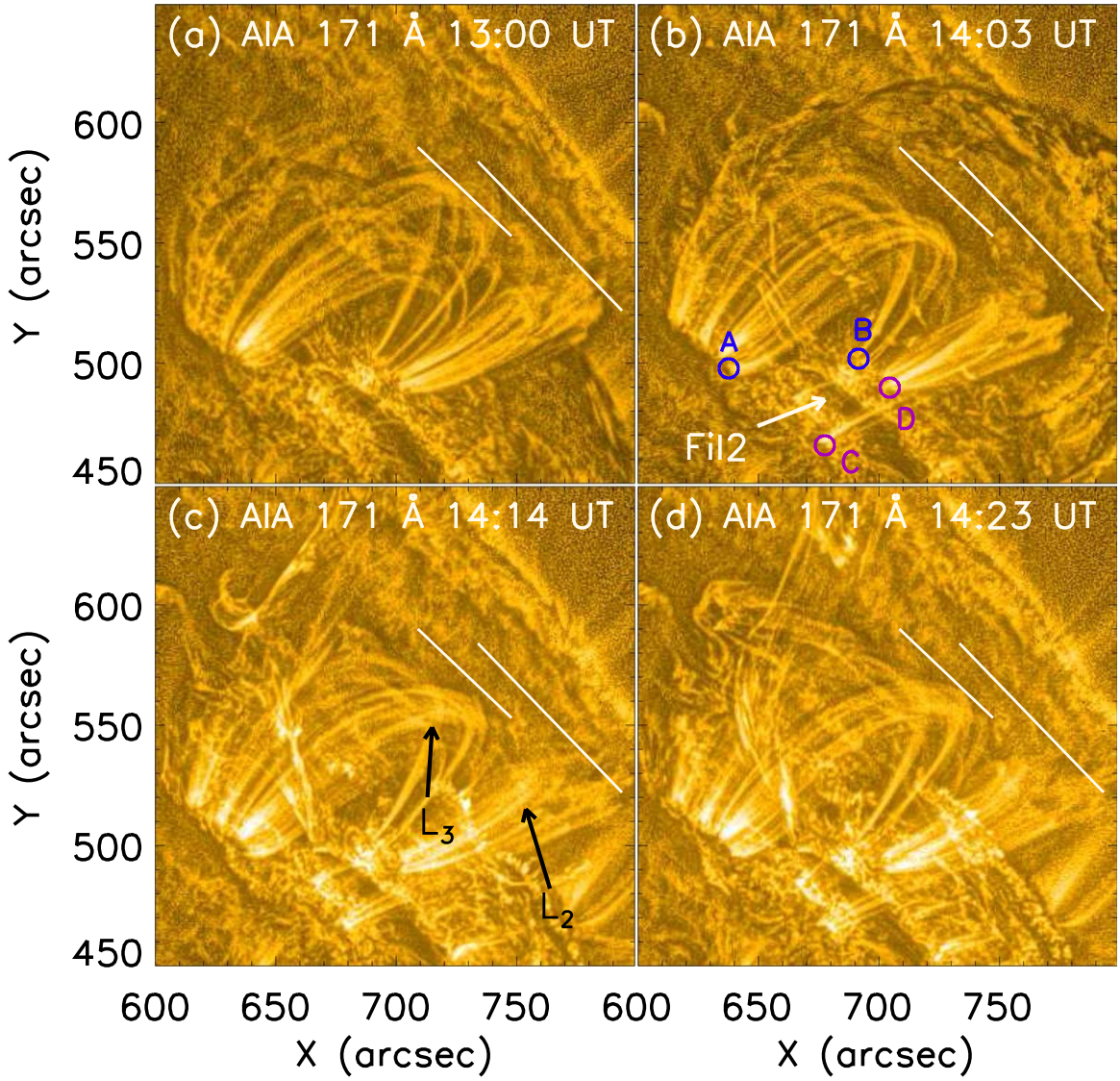

Figure 6. Evolution of the two loop sets located in the neighborhood of the filament Fil_1 eruption and above Fil_2 (seen in the top part of panel (b)). The data are from AIA 171 Å processed with the MGN technique. The white lines are at fixed positions in the solar frame to better visualize the loop evolution. After the filament eruption onset at ≈13:19 UT, the loops first contract (panel (b)), then they expand backward toward their initial locations (panels (c), (d)). The two loop systems are labeled with L_3 and L_2 in panel (c). The selected loop footpoints are marked with A, B, and C, D, respectively, in panel (b), and they are reported in Figure 3(f).

UT (before the eruption onset). These lines are repeated in the next panels with fixed coordinates in the local reference frame, so by taking into account the solar rotation. Then, these lines allow better visualization of the loop evolution. We also refer to the attached movies at AIA 171 and 193 Å wavelengths to view the full evolution of these loops. These movies show that all these loops are contracting in phase. The contraction is maximal about 43 minutes after the filament eruption onset (Figure 6(b)). Later their motions reverse and they expand approximately back to their original positions. No further oscillation is observed.

For a quantitative analysis of these two sets of loops, we show the results obtained along two slices selected to cross the loop tops nearly orthogonally, so along the loop motion. We name these slices S_2 and S_3. They cross the loop sets L_2 and L_3, respectively. The results of these spacetime analyses are presented in Figures 7 and 8 for the AIA 171 and 193 Å data, respectively. We corrected the height projection from the solar rotation. The results with slice S_1, defined in Figures 4(a), are also included in the panels (b). They both confirm the upward motion and velocities of the filament Fil_1 obtained with the 304 Å filter. In contrast, the stable filament Fil_2 is present at a nearly constant position in the lower part of panels (c) of Figures 7 and 8. The upward little drift of Fil_2 is not due to the solar rotation as it is removed. We interpret this drift as follows. This stable filament is in a decaying AR, and cancellation occurs at the PIL, further building up the FR configuration. So the FR is slowly moving up toward a nearby equilibrium. Such slow evolution has been analyzed before for several observed events (e.g., Byrne et al. 2014; Gosain et al. 2016; Chandra et al. 2017).

The loops L_2 crossed by slice S_2 are initially stable up to ≈13:40 UT when they start contracting (Figure 7(c)). At that time, the apex of filament Fil_1 was already moving upward at a velocity ≈6 km s^{-1} (Figure 7(b)). Across slice S_2, the erupting filament Fil_1 is partly masked by the foreground set of loops L_2 present along the line of sight (Figures 6, 7(c)). Fil_1 is observed in absorption before and after the crossing of the contracting loops. The contraction of all the loops starts almost simultaneously

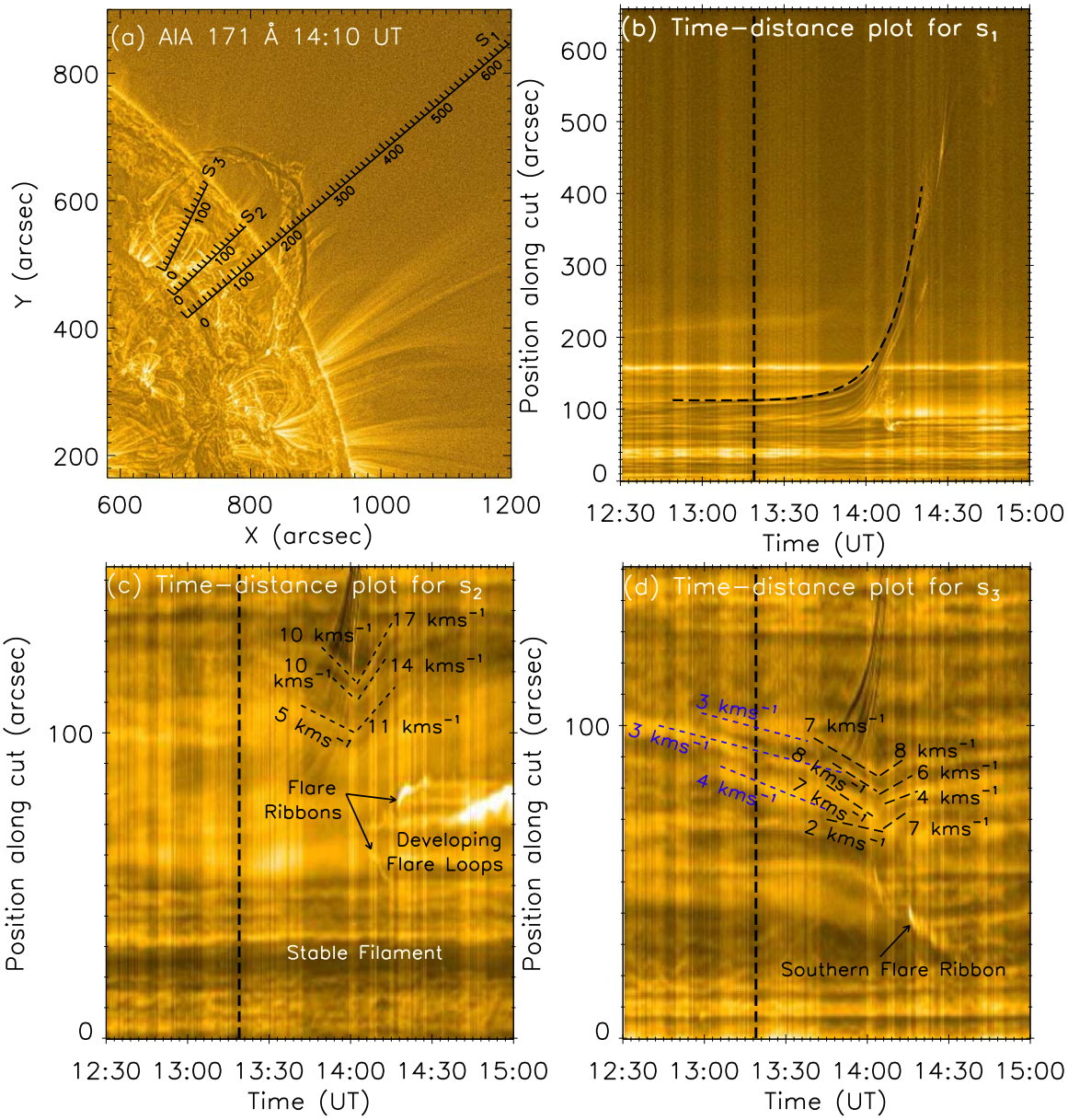

Figure 7. (a) AIA 171 Å image processed with the MGN technique. The location of three slices is shown. Slice S_1 is the same as in Figure 4(a). It monitors the filament height versus time. Slices S_2 and S_3 are monitoring the loop contraction/expansion along the loop systems L_2 and L_3, respectively (see Figure 6). (b) Height-time plot for the filament eruption with the fit of Equation (1) to the AIA 171 data of the filament leading edge added with a dashed line. (c), (d) Height-time plots along slices S_2 and S_3 showing the contraction and expansion of the EUV loops during the filament eruption. The vertical dashed line indicates the approximate onset time of the eruption. The short dashed segments outline the loop contraction/expansion of the loops. The derived mean speeds are added close to each segment. In panel (c), the trace of the flare ribbons and of the developing flare loops are indicated. In both panels (c) and (d). the erupting filament is seen when it emerged from the occulting coronal loops L_2 and L_3.

≈21 minutes after the filament eruption onset. This is in the range of 4–40 minutes of the time difference between the onsets of filament eruption and loop contraction reported before (Shen et al. 2014; Dudík et al. 2016, 2017; Wang et al. 2018; Devi et al. 2021). The speed of the contraction varies from 5–10 km s^{-1}. This contraction continues for a duration of ≈22 minutes. At ≈14:02 UT, these loops change suddenly from contraction to expansion without any significant phase difference between them. The speed of the expansion is in the range of 11–17 km s^{-1}. This expansion speed is higher by a factor of 2 than the contraction speed. The expansion continues at least for 15 minutes, and afterwards these loops L_2 are difficult to detect with the 171 Å filter.

A similar loop evolution is present with AIA 193 Å (Figure 8). The speeds of the contracting and expanding loops are comparable to the one observed in AIA 171 Å. The small difference in velocities could have several origins: the difference in the emitting plasma, the diffuse appearance of the loops, the short and partly different duration of the contraction and expansion phases (as could be observed when enough emitting plasma was present). Finally, one more loop, with similar time evolution than others, is detected in 193 Å (the lower one in Figure 8(c)).

The slice S_3 analyses a different set of loops, L_3, which are located closer to the northern leg of the erupting filament Fil_1 (Figure 7(a)). This loop system has a similar behavior as the

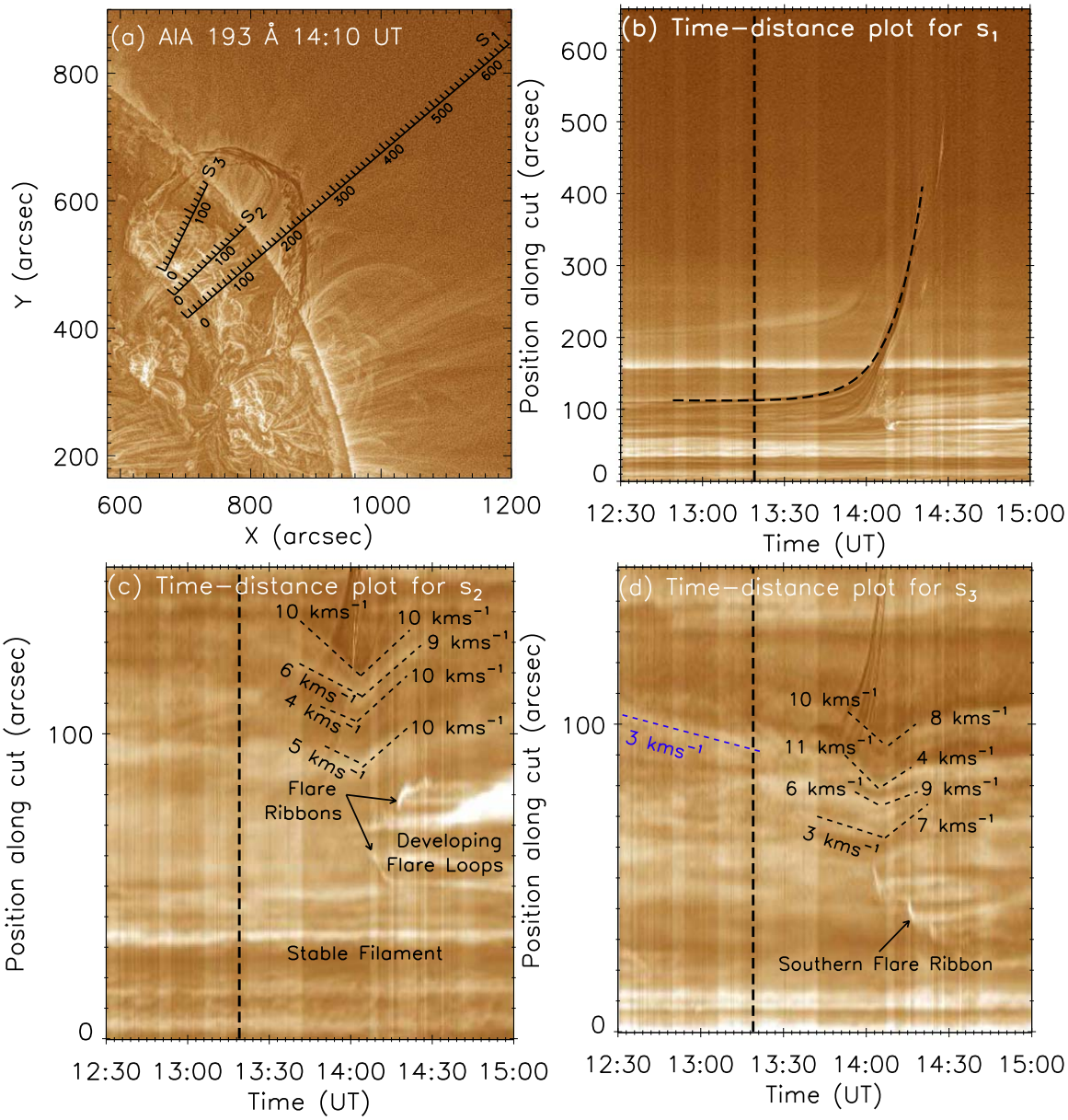

Figure 8. Data of AIA 193 Å processed with the MGN technique and with the same format as Figure 7. (a) AIA 193 Å image with the same slices (S_1, S_2, and S_3) as in Figure 7(a). (b) Height-time plot for the filament eruption with the fit of Equation (1) to the AIA 193 data of the filament leading edge added with a dashed line. The height has a constant projection factor on the plane of the sky. (c), (d) Height-time plots showing the contraction and expansion of the EUV loops after the filament eruption along slices S_2 and S_3. The vertical dashed line indicate the onset time of the eruption. The typical contraction/expansion speeds of the loops are added, as well as the flare traces.

loop system L_2 except that it shows also a contraction before the filament eruption onset. We refer to this contraction as *earlier loop contraction*. This earlier loop contraction can be clearly seen in the panels (d) of Figures 7 and 8 respectively (see also the accompanying movie). This contraction starts between ≈12:30 and 13:00 UT and the computed speed for the earlier contraction is about 3–4 km s^{-1}. Next, about 21 minutes after the eruption onset, the loops in S_3 contract as the ones of slice S_2. The contraction speed in the case of 171 Å varies from 2–8 km s^{-1} which is comparable to the speeds deduced from the 193 Å filter (in the range of 3–10 km s^{-1}). The contraction time for both wavelengths is about 22 minutes. As the loops of S_2, the contraction changes rapidly to an expansion at ≈14:02 UT. The expansion speed varies from 4–8 km s^{-1} in case of 171 Å and from 4–9 km s^{-1} in the case of 193 Å so comparable to the contraction speed. For both contraction and expansion, there is a global tendency of an increasing velocity with height, a tendency which is also present for slice S_2. Next, at the difference with loops L_2, loops L_3 could be followed much longer in time. About 20 minutes after motion reversal, this expansion slows down and it is over by ≈14:27 UT (panels (d) of Figures 7 and 8). No significant evolution is present later on.

The slice S_2 shows also the consequences of the flare reconnection (panels (c) of Figures 7 and 8). The flare ribbons start to significantly brighten and to separate from each other in slice S_2 at ≈14:18 UT, while they are detected starting earlier, at ≈13:59 UT, close to slice S_3 which is coherent with an eruption starting at the end of Fil_1. The flare loops are observed later on, after ≈14:34 UT in S_2. The drift of position observed in panels (c) of Figures 7 and 8 is interpreted as the formation of higher flare loops as magnetic reconnection proceeds. In slice S_3, after 14:00 UT and for an abscissa $< 50''$ there is a

brightening shift to lower S_3 abscissa. We have examined this shift in detail by analyzing the movies and corresponding images. This shift corresponds to the motion of the southern flare ribbon.

3. Physical Interpretation

3.1. Erupting Magnetic Field Configuration

The evolution of the radial magnetic field component is typical on an AR in decay (Figure 3 and associated movie). Magnetic flux is progressively dispersed by super-granules convective cells. This implies that both magnetic polarities of AR 11690are growing in extension. This induced magnetic field cancellations around the photospheric level along the internal PIL of the AR. This evolution is generically expected to build an FR (van Ballegooijen & Martens 1989; Aulanier et al. 2010; Green et al. 2011) where dense plasma could be caught (e.g., Aulanier & Démoulin 1998), forming filament Fil_2.

Photospheric magnetic cancellation is also triggered by the field dispersion at the AR boundary, especially at the PIL between polarities N_1 and P_0. Our observations of cancellation of magnetic flux at the photospheric level below the filaments are consistent with the study of the filament formation of Wang & Muglach (2007). Two of their studied filaments were formed at the periphery of ARs, like Fil_1, while the third one was formed inside a decaying AR like Fil_2. They concluded that the filaments are formed due to the same process of magnetic flux cancellation at PIL. Here, the studied filaments, Fil_1 and Fil_2, are around the same magnetic polarity N_1. Before the eruption it is difficult to set the limit between Fil_1 and Fil_2 but eruption of only Fil_1 favors that they have two separated magnetic configurations.

The main addition to the above magnetic diffusion scenario is the emergence of a magnetic bipole in the leading negative polarity of AR 11690 (Figures 3(b)–(e) and associated movie). This bipole has almost the reverse orientation than the main bipole forming AR 11690 (P_1, N_1). The emerging positive polarity mainly cancels with the outer (westward) part of polarity N_1. This reconnection transfers the negative footpoint from N_1 to the emerging negative polarity. The coronal implication of this reconnection depends on the initial coronal connectivity of N_1. The part closer to the internal PIL of AR 11690 is expected to connect to P_1. In this case the reconnection brings the negative footpoint of the reconnected fields connecting P_1 closer to the internal PIL. This decreases the curvature radius of field lines, then strengthens the stabilizing magnetic tension force of the magnetic configuration supporting filament Fil_2. However, the external part of N_1 is expected to connect P_0 (e.g., as it does with a potential field). In this case the reconnection brings the negative footpoint of the reconnected fields connecting P_0 away from the external PIL. This weakens the stabilizing tension force of the filament Fil_1, then it is an ingredient to bring the magnetic configuration of Fil_1 to eruption. Still, this reconnection was not sufficient since the positive polarity of the emergence canceled and disappeared on the day before Fil_1 eruption. These results are in agreement with the study of Chen & Shibata (2000).

The 3D standard model of eruptive flares is typically developed in a bipolar field modeling an AR with the buildup, then eruption, of an FR formed above the internal PIL (e.g., Aulanier et al. 2010; Janvier et al. 2015). In the case of an external PIL, located at the periphery of an AR, the same model could be qualitatively be applied if a first coronal reconnection forms a sheared arcade over this PIL, as shown by Török et al. (2018). The following evolution is mainly driven by the diffusion of magnetic polarities, as for the case of an internal PIL. The main difference at this stage is an expected slower process as the spatial region involved around the external PIL is large while convective cells have typically the same speed.

When the magnetic configuration reaches an instability (as evidenced by the exponential growth of the filament height), the filament trace an erupting FR structure well observed both with SDO/AIA and STEREO A/EUVI 304 Å filters (Figures 4 and 5 and related movies). Reconnection behind the erupting FR leads to the formation of a flare loop arcade ending in two J-shaped flare ribbons observed in EUV wavelengths. They separate as a function of time as excepted in the standard 3D eruption model. Then, we conclude that, while located at the periphery of an AR, the eruption of Fil_1 has all the characteristics expected with the 3D standard model of eruptive flares built for eruptions located in the core of ARs. The main differences are slower processes both for the formation and the ejection of the FR (due to a weaker magnetic field, so weaker forces).

3.2. Contracting and Expanding Loops

The loop system L_3 (panels (d) of Figures 7 and 8) shows the earlier contraction as mentioned in Section 2.4. The data presented here provide no clue about this contraction. We observe small brightenings at the base of loop system L_3 before the eruption and a short description of our analysis is presented in Appendix since this could be interesting for further studies on the subject. In present observations the sets of contracting loops, L_2 and L_3, mostly recover the original heights they had when the fast contraction started (Figure 6, panels (c) and (d) of Figures 7 and 8). This evolution is different than for loops located in the elbow of AR sigmoids as, the expansion following contraction is frequently not able to recover the pre-eruption location (e.g., Liu et al. 2012; Simões et al. 2013; Shen et al. 2014; Wang et al. 2018), while in some cases it does (e.g., Dudík et al. 2017). This behavior is expected for loops at a remote filament channel where no energy release happens. A possibility is that the eruption generates a coronal wave which first pushes the loops L_2 and L_3 downward, then the loops recover their initial positions after the coronal wave passage. Indeed, there have been previously studied cases where loops oscillate during the crossing of a coronal wave (e.g., Ballai 2007; Guo et al. 2015; Fulara et al. 2019). In these studies, the oscillations have at least one cycle. In the present case, a weak coronal wave is associated with the eruption as visible at http://suntoday.lmsal.com/sdomedia/SunInTime/2013/03/16/AIAtriratio-211-193-171-2013-03-16T1200.mov.mp4. Due to the weak nature of the coronal wave, it is very difficult to estimate if it interacted with the loops and at which time. The main observational constraint is that the loops have only half period oscillation with a triangular shaped amplitude. This is far from the behavior expected from an unforced oscillator, as summarized, e.g., in Figures 2 and 4 of Russell et al. (2015). The observed triangular shape in Figures 7 and 8 is also well different from oscillations observed in other events (e.g., Gosain 2012; Liu et al. 2012; Simões et al. 2013). Then, an excitation of the loops by a coronal wave is doubtful.

An additional possibility for the origin of the loop contraction and expansion is a perturbation by the lateral

expansion of the erupting flux of the filament. It is known that some eruptions show a so-called overexpansion, a stronger growth of the minor radius (thickness) of the erupting flux compared to the major radius (height) (Patsourakos et al. 2010a, 2010b; Veronig et al. 2018). In the case of Veronig et al. (2018), the lateral overexpansion of the CME bubble first pushes neighboring loops to the side, which leads to very clear oscillations. Subsequently, the bubble acquires a mushroom-like shape, which presses some loops to the north of the eruption downward, followed by a recovery of the loops to the original height. Such behavior was so far seen preferentially in fast or impulsive eruptions. However, a similar dynamics in slower eruptions, like the case here, might nevertheless be possible. Since the perturbation is temporary, a return of the loops to their original position would result naturally.

This event shows, as expected by filament models, that the erupting flux is much thicker and extends much higher than the filament in the hotter channel 211 Å. A diffuse front is seen to rise synchronously with the filament at nearly twice the height (panel (j) of Figure 1). The synchronous motion suggests that the diffuse front is part of the erupting flux, probably at its top edge. This implies that most of the erupting flux is already higher than the loops L_2 and L_3 when their contraction begins. The lateral expansion of the flux at this stage should perturb the flux above these loops. When, as the overlying flux is pushed sideward by the CME bubble, the loops may experience a sideward and downward push. Another possibility of this moving diffuse front at the top of the erupting FR can be formed by the erupting FR, which collects, compress and heats surrounding coronal plasma (and magnetic field too) in front of the FR. So it could not be a part of the erupting flux but coronal plasma collected on the way. It is likely the beginning of a sheath formation, a structure well observed in situ in front of magnetic clouds and more generally ejecta far away from the Sun.

We next analyze how other proposed mechanisms may explain these observations. The implosion conjecture is difficult to test since it was so far not quantitatively formalized and moreover its physical base changed (e.g., from a driver to a consequence of the eruption, see Section 1). Indeed, this conjecture would have to explain how the loop contraction could occur above the stable filament Fil_2 located inside an AR, while the eruption of another filament Fil_1 occurs at the leading border of the same AR. This requires an analysis, with a numerical simulation, which is beyond the scope of the present study. Still, the observations show that the northern end of filament Fil_1 enters slightly within the AR, and reach an end location below L_3 loops. Then, the eruption of Fil_1 is clearly involved in this loop contraction while we cannot provide elements in support of the implosion conjecture. Even more, the evolution of L_2 loops above the stable filament Fil_2 and the return of the loops to their initial position are not within the framework of the implosion conjecture.

The loop contraction model of Zuccarello et al. (2017) explained loop contraction by the development of MHD vortexes that develop on the sides of an erupting FR. The loop contraction, then expansion, occurs in the field lines overlying the footpoints of the FR. The numerical simulations study the instability of an FR located in a bipolar field simulating a simple and isolated AR. This configuration is closer to the magnetic configuration of and above the stable filament Fil_2, as compared with that of the erupting filament Fil_1. Still, following the strongly bent PIL, the contraction/expansion occur on the loops, which are next to the northern footpoint of the erupting FR. Then, the main difference with the simulations of Zuccarello et al. (2017) is that the PIL is so bent that the contracting loops appear on one lateral side, rather than in the continuation, of the erupting filament. Still, an MHD simulation with the observed multipolar configuration (Figure 3) is needed to test the possibility that MHD vortexes develop and imply the loop contraction/expansion as found before with a simple bipolar magnetic configuration.

4. Conclusion

We analyze a filament eruption of 2013 March 16 located close to the west limb. The filament, Fil_1, was located between the leading polarity of a decaying AR and a westward remnant dispersed polarity of opposite sign. In this weak magnetic field environment no GOES flare has been reported to be associated with this eruption. Still, we report an arcade of flare loops and two separating J-shaped flare ribbons on the opposite sides of the PIL of the erupting filament. Later on, the eruption leads to a CME with moderate speed (about 800 $km\,s^{-1}$). All these observational characteristics fit well within the standard 3D model of solar eruptions (Section 1).

The dynamics of the erupting filament is well fitted with a model adding linear and exponential increases of height with time. This quantifies two erupting phases: a slow-rise and an acceleration phase, which characterize two different physical mechanisms. A slow rise is indeed expected to occur as a consequence of the observed cancellation of the photospheric magnetic field at the PIL. This process is expected to build an FR which is progressively rising in height toward a new equilibrium. Recurrent brightenings and restructuring are observed at the northern footpoint of the filament during this phase. Next, the exponential growth of height during the acceleration phase characterizes an instability, which is likely the torus instability since no significant writhing of the erupting filament is observed (as would be present for a kink instability). The onset of the instability is estimated with the time when the exponential growth of the upward velocity becomes significant on top of the previous nearly constant velocity. Another remarkable aspect of the filament eruption was the observations of the drift of southern footpoints of the erupting FR, which could be explained by the interchange reconnection of the erupting configuration with the confront magnetic loops of a neighboring AR. Moreover, we also observe the split of the eruptive FR above the southern footpoints with plasma tracing the magnetic connections to two separated magnetic polarities.

Another filament, Fil_2, is present along the internal PIL of the AR. The northern ends of the filaments are close by, so that both filaments encircle almost the leading polarity of the AR. It is then remarkable that Fil_2 stays undisturbed while Fil_1 is erupting. About 21 minutes after Fil_1 eruption onset, the loops L_3 suddenly accelerate their contraction speed by a factor of 2–3. At the same time the initially stable southern loops L_2, located above Fil_2, contract in a similar way. Then, the full coronal loop system contract for a period of 22 minutes. Later on, the loop motion reverses suddenly, then they expand for a period of 20–25 minutes. The amplitude of the contraction is between 10″and 20″ . Then, this evolution is well resolved both spatially and temporally by SDO/AIA observations. Both the contraction and expansion were observed in phase in the full loop arcade on a significant range of projected heights range

(about 70″). Afterwards, these loops set into a stable configuration close to their original positions at the start of the fast contraction phase. The return of the loops to the original position is naturally expected because they pass over the end point of Fil_1 and over Fil_2, where no or only minimal energy release is expected to occur and the post-eruption equilibrium should be close to the pre-eruption equilibrium.

The characteristics of the loop contraction/expansion in this eruption contrast with previous studies. First, the loop arcade is located above a stable filament and extends up to one end of another erupting filament. Second, the stable filament is located mostly parallel to the erupting one. Third, the stable and erupting filaments are on the same PIL encircling the leading PIL of an AR in decay. Finally, the loop evolution starts with a contraction followed by an expansion recovery phase. This half period oscillation with a triangular shape is an original characteristic of the present event. All these characteristics make this studied event challenging for the models of loop contraction since such magnetic configuration was not observed or modeled before. In particular, this case is different than the one simulated by Zuccarello et al. (2017) where the eruption occurs in the core of the simulated AR, while in present observations the eruption occurs at the leading border of the AR. In summary, numerical simulations are needed with a broader variety of magnetic configurations in order to understand the results of present observations. In particular, it is worth studying how strongly the results are depending on the bending of PIL, so on the fully 3D aspects of the involved magnetic configuration. Such studies can also allow for the better separation of the characteristics of the different models proposed so far to interpret the contraction and expansion of coronal loops.

We recognize the collaborative and open nature of knowledge creation and dissemination, under the control of the academic community as expressed by Camille Noûs at http://www.cogitamus.fr/indexen.html. The authors thank the open data policy of the SDO and STEREO teams. RC acknowledges the support from Bulgarian Science Fund under Indo-Bulgarian bilateral project, DST/INT/BLR/P-11/2019. P.D. is supported by CSIR, New Delhi. We thank the reviewers for their constructive comments and suggestions. We thank Dr. H. Morgan for providing the MGN code.

Appendix
Earlier Loop Contraction

In order to understand the earlier contraction of loop system L_3 (panels (d) of Figures 7 and 8), we studied based difference movies of AIA 304 and 171 Å without and with MGN technique applied before subtracting the image at 12:30 UT. A main brightening episode starts at 12:42 UT and is illustrated in the left panels of Figure A1 in the middle of its duration. This local event is associated with local plasma motions indicating a local restructuring of the magnetic field of the northern end of filament Fil_1. A second brighter event started at 13:30 UT in a close by location, while more extended both north, along Fil_1, and southward inside the AR (Figure A1, right panels). It shows that, at the beginning of eruption, Fil_1 was entering slightly inside the AR (as drawn in Figure 3(d)). This event is the activation and reconfiguration of Fil_1 northern end. The start of this event is later by at least 11 minutes than the eruption onset define in Figure 4(b) (Section 2.3). These local events are best seen in 304 Å, while they are also present in 171 Å, which allows us to locate them well with respect to the loops L_3 (Figure A1, bottom panels). We conclude that these brightenings are the only indications present in the data of magnetic reconfiguration occurring in the vicinity of loops L_3 during the linear and early exponential phases of the filament rise. Then, the data provide no clue about the earlier contraction of loop system L_3. This earlier contraction is possibly associated with the upward motion of the magnetic configuration of Fil_1 in the linear phase. In this case, it has the same physical origin as the contraction present later on in the exponential phase (panels (c) and (d) of Figures 7 and 8).

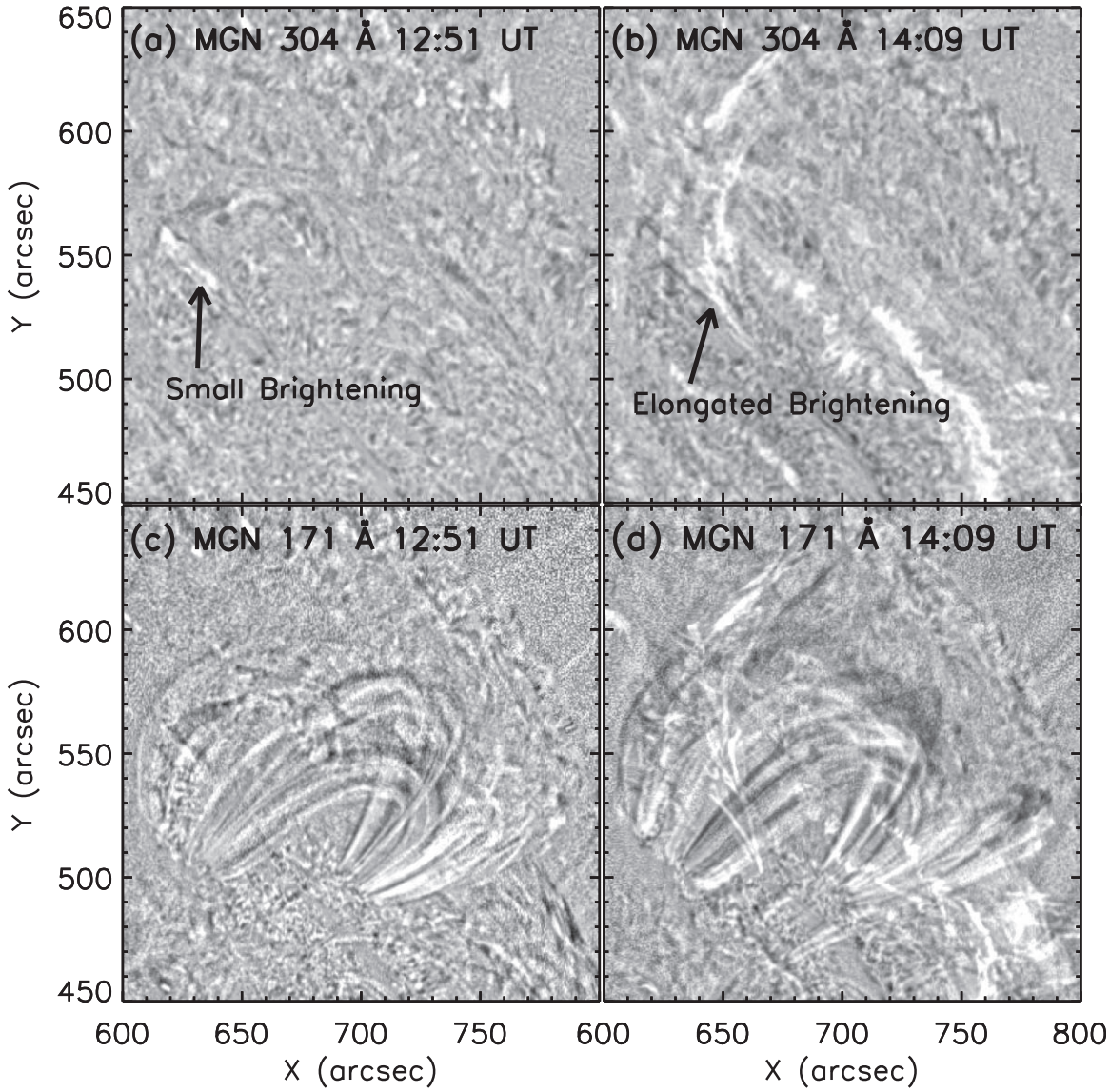

Figure A1. MGN base difference images of AIA 304 and 171 Å at 12:51 and 14:09 UT. The base time for these images is 12:30 UT. The small brightening before the eruption and the elongated brightening during the eruption are shown in panels (a), (c) and (b), (d), respectively. These brightenings are located at the end of filament Fil_1, close and partly below the L_3 loop system (bottom panels). An animation of this figure is available. The animation starts at 12:30 UT and end at 15:00 UT. The real-time duration of the animation is 25 s.

(An animation of this figure is available.)

ORCID iDs

Ramesh Chandra https://orcid.org/0000-0002-3518-5856
Pascal Démoulin https://orcid.org/0000-0001-8215-6532
Pooja Devi https://orcid.org/0000-0003-0713-0329
Reetika Joshi https://orcid.org/0000-0003-0020-5754
Brigitte Schmieder https://orcid.org/0000-0003-3364-9183

References

Amari, T., Aly, J. J., Mikic, Z., & Linker, J. 2010, ApJL, 717, L26
Antiochos, S. K., Dahlburg, R. B., & Klimchuk, J. A. 1994, ApJL, 420, L41
Antiochos, S. K., DeVore, C. R., & Klimchuk, J. A. 1999, ApJ, 510, 485
Aulanier, G., & Démoulin, P. 1998, A&A, 329, 1125
Aulanier, G., Démoulin, P., Mein, N., et al. 1999, A&A, 342, 867
Aulanier, G., & Schmieder, B. 2002, A&A, 386, 1106
Aulanier, G., Török, T., Démoulin, P., & DeLuca, E. E. 2010, ApJ, 708, 314
Ballai, I. 2007, SoPh, 246, 177
Ballai, I., Douglas, M., & Marcu, A. 2008, A&A, 488, 1125
Byrne, J. P., Morgan, H., Seaton, D. B., Bain, H. M., & Habbal, S. R. 2014, SoPh, 289, 4545
Carmichael, H. 1964, NASSP, 50, 451
Chandra, R., Filippov, B., Joshi, R., & Schmieder, B. 2017, SoPh, 292, 81
Chandra, R., Pariat, E., Schmieder, B., Mandrini, C. H., & Uddin, W. 2010, SoPh, 261, 127
Chandra, R., Schmieder, B., Aulanier, G., & Malherbe, J. M. 2009, SoPh, 258, 53
Chen, P. F., & Shibata, K. 2000, ApJ, 545, 524
Cheng, X., Zhang, J., Kliem, B., et al. 2020, ApJ, 894, 85
Démoulin, P., Priest, E. R., & Lonie, D. P. 1996, JGR, 101, 7631
Devi, P., Démoulin, P., Chandra, R., et al. 2021, A&A, 647, A85
Dudík, J., Lörinčík, J., Aulanier, G., Zemanová, A., & Schmieder, B. 2019, ApJ, 887, 71
Dudík, J., Polito, V., Janvier, M., et al. 2016, ApJ, 823, 41
Dudík, J., Zuccarello, F. P., Aulanier, G., Schmieder, B., & Démoulin, P. 2017, ApJ, 844, 54
Forbes, T. G., & Acton, L. W. 1996, ApJ, 459, 330
Fulara, A., Chandra, R., Chen, P. F., et al. 2019, SoPh, 294, 56
Georgoulis, M. K., Nindos, A., & Zhang, H. 2019, RSPTA, 377, 20180094

Gibson, S. E., & Fan, Y. 2006, ApJL, 637, L65
Gosain, S. 2012, ApJ, 749, 85
Gosain, S., Filippov, B., Ajor Maurya, R., & Chandra, R. 2016, ApJ, 821, 85
Green, L. M., Kliem, B., & Wallace, A. J. 2011, A&A, 526, A2
Green, L. M., Török, T., Vršnak, B., Manchester, W., & Veronig, A. 2018, SSRv, 214, 46
Guo, Y., Erdélyi, R., Srivastava, A. K., et al. 2015, ApJ, 799, 151
Hirayama, T. 1974, SoPh, 34, 323
Hori, K. 2000, ApJ, 543, 1011
Howard, R. A., Moses, J. D., Vourlidas, A., et al. 2008, SSRv, 136, 67
Hudson, H. S. 2000, ApJL, 531, L75
Janvier, M., Aulanier, G., & Démoulin, P. 2015, SoPh, 290, 3425
Joshi, B., Veronig, A., Cho, K. S., et al. 2009, ApJ, 706, 1438
Kay, C., Opher, M., & Evans, R. M. 2015, ApJ, 805, 168
Kippenhahn, R., & Schlüter, A. 1957, ZA, 43, 36
Kliem, B., & Török, T. 2006, PhRvL, 96, 255002
Kliem, B., Török, T., Titov, V. S., et al. 2014, ApJ, 792, 107
Kopp, R. A., & Pneuman, G. W. 1976, SoPh, 50, 85
Labrosse, N., Heinzel, P., Vial, J. C., et al. 2010, SSRv, 151, 243
Lemen, J. R., Title, A. M., Akin, D. J., et al. 2012, SoPh, 275, 17
Li, Y. P., & Gan, W. Q. 2006, ApJL, 644, L97
Lin, J., & Forbes, T. G. 2000, JGR, 105, 2375
Liu, R., Liu, C., Török, T., Wang, Y., & Wang, H. 2012, ApJ, 757, 150
Lörinčík, J., Dudík, J., & Aulanier, G. 2019, ApJ, 885, 83
Mackay, D. H., Karpen, J. T., Ballester, J. L., Schmieder, B., & Aulanier, G. 2010, SSRv, 151, 333
Moore, R. L., & Sterling, A. C. 2006, in Solar Eruptions and Energetic Particles, ed. N. Gopalswamy, R. Mewaldt, & J. Torsti, 165 (Washington DC: American Geophysical Union), 43
Morgan, H., & Druckmüller, M. 2014, SoPh, 289, 2945
Panasenco, O., Martin, S. F., Velli, M., & Vourlidas, A. 2013, SoPh, 287, 391
Parenti, S. 2014, LRSP, 11, 1
Patsourakos, S., Vourlidas, A., & Kliem, B. 2010a, A&A, 522, A100
Patsourakos, S., Vourlidas, A., & Stenborg, G. 2010b, ApJL, 724, L188
Patsourakos, S., Vourlidas, A., Török, T., et al. 2020, SSRv, 216, 131
Pesnell, W. D., Thompson, B. J., & Chamberlin, P. C. 2012, SoPh, 275, 3
Priest, E. R., Hood, A. W., & Anzer, U. 1989, ApJ, 344, 1010
Russell, A. J. B., Simões, P. J. A., & Fletcher, L. 2015, A&A, 581, A8
Schmieder, B., Démoulin, P., & Aulanier, G. 2013, AdSpR, 51, 1967
Schou, J., Scherrer, P. H., Bush, R. I., et al. 2012, SoPh, 275, 229
Shen, J., Zhou, T., Ji, H., et al. 2014, ApJ, 791, 83
Simões, P. J. A., Fletcher, L., Hudson, H. S., & Russell, A. J. B. 2013, ApJ, 777, 152
Sturrock, P. A. 1966, Natur, 211, 695
Sui, L., Holman, G. D., & Dennis, B. R. 2004, ApJ, 612, 546
Sun, X., Hoeksema, J. T., Liu, Y., et al. 2012, ApJ, 748, 77
Titov, V. S., Downs, C., Mikić, Z., et al. 2018, ApJL, 852, L21
Titov, V. S., Downs, C., Török, T., et al. 2021, ApJS, 255, 9
Török, T., & Kliem, B. 2005, ApJL, 630, L97
Török, T., Leake, J. E., Titov, V. S., et al. 2018, AGUFM, 2018, SH12A–04
Török, T., Panasenco, O., Titov, V. S., et al. 2011, ApJL, 739, L63
van Ballegooijen, A. A., & Martens, P. C. H. 1989, ApJ, 343, 971
van Driel-Gesztelyi, L., Baker, D., Török, T., et al. 2014, ApJ, 788, 85
Veronig, A. M., Podladchikova, T., Dissauer, K., et al. 2018, ApJ, 868, 107
Wang, J., Jiang, C., Yuan, D., & Zou, P. 2021, ApJ, 911, 2
Wang, J., Simões, P. J. A., & Fletcher, L. 2018, ApJ, 859, 25
Wang, Y. M., & Muglach, K. 2007, ApJ, 666, 1284
Williams, D. R., Török, T., Démoulin, P., van Driel-Gesztelyi, L., & Kliem, B. 2005, ApJL, 628, L163
Wills-Davey, M. J., & Thompson, B. J. 1999, SoPh, 190, 467
Zemanová, A., Dudík, J., Aulanier, G., Thalmann, J. K., & Gömöry, P. 2019, ApJ, 883, 96
Zhou, T., Ji, H., & Huang, G. 2008, AdSpR, 41, 1195
Zhou, T.-H., Wang, J.-F., Li, D., et al. 2013, RAA, 13, 526
Zuccarello, F. P., Aulanier, G., Dudík, J., et al. 2017, ApJ, 837, 115